ELSEVIER

Moving towards materials with humanoid functionality: Sensing their speech with piezoelectric nanowebs

Giulia Lanzara *, **Krishna Chytanya Chinnam, Erika Magnafico, Federico Fabriani**

Department of Civil Engineering, Computer Science and Aeronautical Technologies, University of Rome, RomaTre, 00146, Rome, Italy

The new concept of "humanoid matter" is presented by exploring if the sound emitted by materials embeds phonetic signatures. This overarching topic is here narrowed down to the analysis of the acoustic sound emitted by the sudden hierarchical rupture of microfibers in a composite. While such a low-energy pain-like event for the material is hardly detected with the most advanced structural health monitoring systems, here it is accurately captured (i.e., "listened") with a piezoelectric nanoweb that weighs less than 0.25% than the reference microphone. As humans react to pain with an unarticulated voice pattern, the composite delivers an unvoiced/voiced pattern when suddenly damaged. The phonetic analysis demonstrates the feasibility of using the energy released by a mechanical failure as sound source (i.e., vocal cords) that excites the acoustic resonances of the material (i.e., vocal tract). Differently from healthy humans, the progressive failures slightly modulate the vibration speed of the vocal cords (pitch) due to the stiffness changes of the vocal tract which thus modifies its sound shaping action. The sound signals from the material carry the phonetic fingerprints of the microdamage. This work represents a first step towards materials that possess humanoid functionalities which can potentially revolutionize human-object interaction.

Keywords: Sound; PVDF; Electrospun; Electrospinning; Damage; Piezoelectric mat; Web; Speech; Phonetic; Microwires; Humanoid matter; Material Phonetics; Piezoelectric Nanowebs; PVDF electrospun fibres; Structural Health Monitoring; Acoustic Emission Sensing; Microdamage Detection; Phonetic Analysis of Materials; Mechano-Acoustic Response; Sound-Emitting Materials; Speech-Inspired Sensing; Bioinspired Materials; Piezoelectric Acoustic Sensors; Material Damage Characterization; Advanced Non-Destructive Testing (NDT); Multiscale Failure Detection; Non-Contact Damage Monitoring

Introduction

In this exciting new era, "Things" are borrowing their intelligence from their interconnection with the web to reach, via the web, other objects or humans. This concept is known as "internet of things". "Things" are objects that cover the full spectrum of applications ranging from tangible and intangible daily life products to structures and devices. It is actually true, however, that the heart of any object is in its constituting matter without which the object, including those that are intangible, would not exist. A significant step forward could then be achieved by conceiving "humanoid things" formed by a "humanoid matter" that, through "speech" can directly interact with humans. This paper tries to address this topic for the first time in the literature by investigating whether the sound emitted by materials can embed a phonetic language, which, if properly interpreted, may revolutionize the interaction of human-matter and thus of human-objects. The intimate emotions of matter are however diverse and complex for addressing in a single study. As humans may speak, scream, or emit a speechless or burst sound when they feel pain or when they get injured, materials may be made to mimic the idea of feeling pain when they break down or are overstressed. We thus investigate the phonetics of the "material pain" taking advantage of the known concept that

* Corresponding author.
E-mail address: Lanzara, G. (giulia.lanzara@uniroma3.it)

https://doi.org/10.1016/j.mattod.2025.01.003

materials emit sound upon breaking. Here this is done by implementing an unconventional mechano-phonetic approach applied to microdamage occurrence, whose detection is still considered one of the greatest challenges in the field of Structural Health Monitoring (SHM) systems for the reasons described below. In other words, by exploring the new concept of the materials' spoken language, we also provide an exotic technological solution to detect ultra-small damage via humanoid matter. This is important since in the last decade, the use of SHM systems underwent an incredible expansion in all fields that require lightness, safety, reliability and durability of structures, materials or devices. When integrated into structures, machines or devices, such systems are designed to monitor over time their health often with respect to the surrounding environment (e.g, temperature, humidity [1,2]). The most recent approaches take advantage of artificial intelligence (e.g. machine learning [3], deep learning [4] or intelligent computational methods [5]) to strengthen the system efficiency and reliability. Several types of SHM systems have been proposed in the literature and are available in the market [6].

The fundamental idea is that an array of devices is surface mounted or embedded in such a way that they gather information about the hosting structure. The system may include both active and passive elements to monitor the structure as needed, such as using acoustic emission methods [7,8] (e.g., with piezoelectrics) [9–12], or solely passive sensors to continuously listen to the structure over time (e.g., chemical sensors, strain gauges [13], fiber optics [14–16], accelerometers [17], wireless multifunctional sensors [9] or, more recently, nanostructured piezoresistive [18–21] and piezopolymer sensors [22–29]). The mapping capability of these systems is strongly related to the density of acquisition points: the larger the density of the embedded devices, the higher is the mapping resolution [15,16,30]. Lighter, denser, and non-invasive arrays which ideally require negligible installation costs and non-contact monitoring approaches, represent the state-of-the-art of the most advanced SHM systems ever presented in the literature. In the first case, highly stretchable substrates are functionalized with miniaturized devices and electronics to deliver prefabricated and highly stretchable sensor networks [31,32]. Instead, in the second case, the most recent non-contact approaches rely entirely on the acquisition of multiple images [33,34], which can also be captured in ultra-fast mode for dynamic analyses [35]. These approaches also include the acquisition of temperature maps [36], laser scanning [37–39], air-coupled laser ultrasound [40], laser excited acoustic shearography [41], acoustic excitations through speakers [42], and radar detections [43] to reconstruct the structural evolution over time. Combining non-contact approaches with artificial intelligence also represents a new avenue [44]. In other words, non-contact systems acquire information only from the outer surface, making them ineffective in detecting internal damage, which can only be addressed using complex global structural models. In conclusion, since damage typically initiates locally at the nano/micro-scale, both contact and non-contact technologiesl remain inadequate for detecting damage at its earlies stages [45].

By taking advantage of the known concept that materials emit sound during transitions between equilibrium states, such as crack formation or phase transformations [46], alternative monitoring systems based on acoustic sensing via microphones have been proposed. These methods include analyzing acoustic radiation from vibrating panels [47] or sandwich beams [48], studying elastic structure interaction with acoustic waves [49], and assessing the vibro-acoustic response of helicopters [50]. Additionally, sound-based structural health monitoring (SHM) systems [51] have been implemented for damage detection [52,53] in various applications, including masonry structures [54], variations in plates thickness [55], local delamination in fiber-reinforced composites [56], loose bolts [57,58], induction motors [59,60], bridges [61,62], wind turbines [63–68], concrete structures [69] and biomedical applications [70] using MEMS microphones. However, the size of damage represents again a critical factor. As damage decreases - as in the case of incipient failures - it leads to a variety of effects: a reduction of the area that emits energy and the generation of highly localized impulsive vibrations arising out from nano/micro-sized sound sources. Such ultra-small sources produce extremely low-pressure levels, making detection challenging. While highly sensitive microphones are required, they are usually expensive, relatively massive, large-in-scale, difficult to be coupled with the structure and to be effectively isolated from environmental noise.

In this study, a nanostructured piezoelectric web, ("piezoweb") that is as light as a feather [71–75] and highly sensitive [74,75], is used to explore the exotic possibility of letting the material "speak" through the sound that it generates, investigating, in particular, if the sound signals encode speech-related damage information. The approach involves "listening" to the material and interpreting its "language" as damage recognition. This approach relies on the close cooperation between the piezoweb, which functions as an acoustic sensor, and the sound-emitting material that plays the role of sound source. Together, they are essential to advancing the concept of a "speaking material". The demonstration is here restricted to a material with a dominant micro-scaled failure mode, which is accurately detected and found to carry key phonetic fingerprints. This concept can be extended to various materials, failure mechanisms, stress/strain states, and monitoring parameters or properties, allowing them to be reinterpreted in terms of material phonetics and speech.

Incipient damage detection via sound monitoring

Micro-damage detection via sound monitoring is validated by inducing damage in a carefully selected composite sample expected to exhibit a single failure mode, avoiding the complexity of multi-modal failure mechanisms. Commercial composite strips, made of polyethylene terephthalate (PET) micro-filaments embedded in a polyethylene (PE) matrix, were used in the study assuming the conceptual role of sound-emitting material. The PET filaments were arranged both longitudinally and transversely with respect to the sample length, creating a distinct pattern depicted schematically in Fig. 1**(a)**.

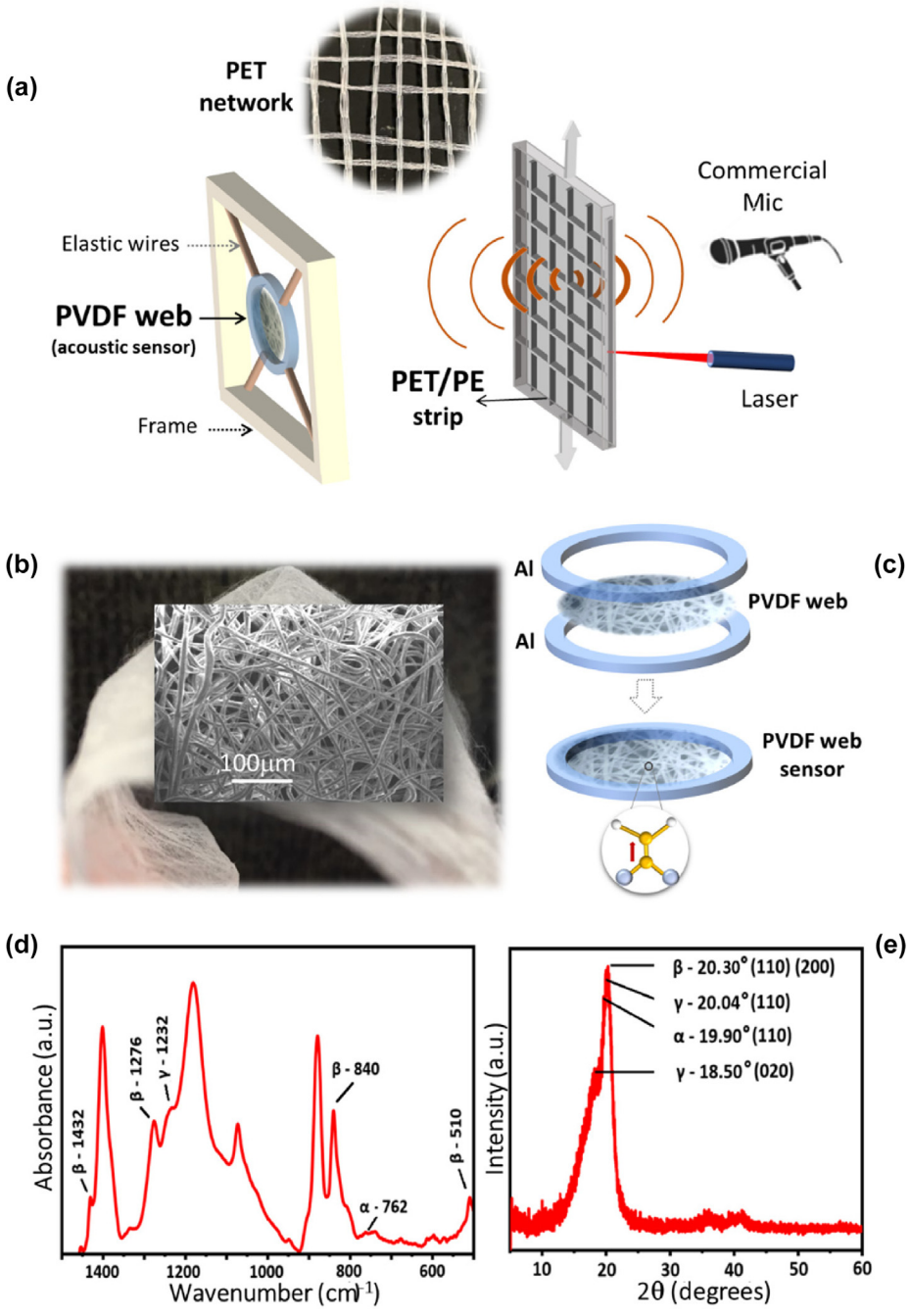

FIG. 1

(a) Image of a PET network that forms the PE/PET composite strip and test set-up for the incipient damage detection comprising a mechanically suspended piezoweb formed by an electrospun Polyvinylidene Fluoride mat (PVDF web), a laser vibrometer and a commercial microphone as non-contact monitoring devices; (b) Optical image of an electrospun piezoweb highlighting the lightness and flexibility while being held and bent. The inset shows an SEM image of the PVDF web morphology without any sample treatment. The random distribution of the electrospun microfibers forms a nanoporous structure which enhances the interaction with the vibrating air particles; (c) Schematic of the acoustic piezoweb sensor (PVDF web sensor) which comprises top and bottom annular shaped Al electrodes which form a sandwich structure. The electrospinning process defines the orientation of the β and γ crystalline phases, perpendicularly to the PVDF web plane (schematically represented). The annular electrodes collect the generated charges. Such electrode shape does not allow to fully collect all charges but has the advantage of leaving the central part of the membrane be free-to-vibrate; (d) FTIR spectrum acquired with a resolution of 4, a gain of 1 and 32 scans, range 500–1500 cm^{-1}; (e) XRD spectrum performed on a 2 cm × 2 cm PVDF membrane.

The composite strips underwent failure via tensile loading at a speed of 2.4 mm/s.

Fig. 2(a) illustrates a typical response, while Fig. 1(a) provides a schematic representation of the test setup. A typical response is characterized by a linear phase followed by nonlinear softening up to a maximum tensile load within 43 N and 48 N. A further material softening is then followed either by a macroscopic sudden failure or by consecutive drops of force towards a flat plateau

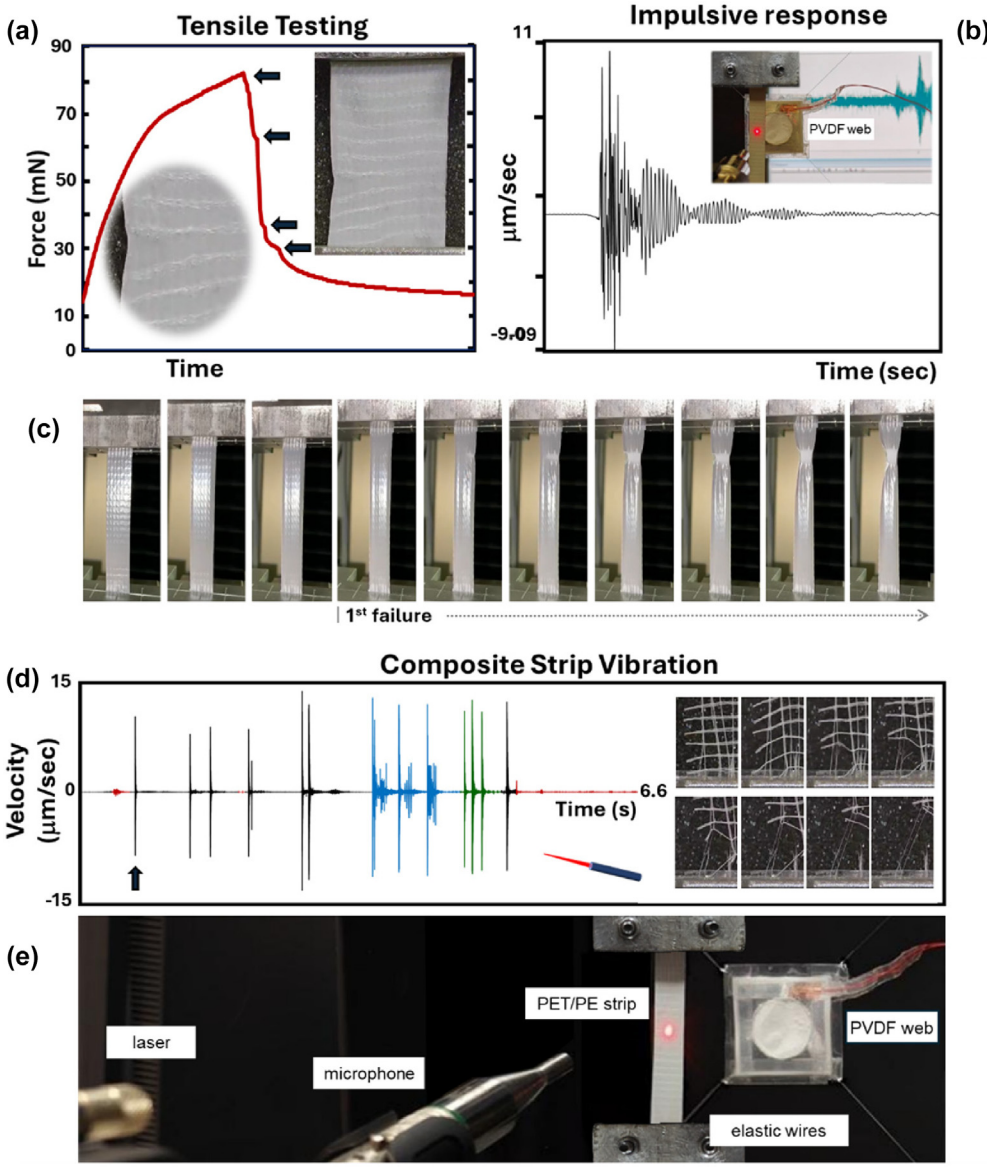

FIG. 2

(a) Example of a tensile response of the composite strip (180 µm thick, 6 cm long and 1 cm wide) in terms of Force evolution over Time in response to a linearly increasing applied displacement. The arrows highlight some of the energy releases due to two types of microfilaments breaking highlighted in (Fig. 3); (b) higher magnification of the first impulsive peak indicated with the grey arrow in (c) which highlights the vibration noise that characterizes the isolated high amplitude peaks. The inset shows a picture of the PVDF web while being monitored with the laser and the simultaneous data acquisition of the PVDF web data; (d) consecutive frames of a composite strip during tensile testing highlighting the onset of filaments failure and plasticization of the PE matrix; (d) Time domain response of the composite strip, in terms of velocity, acquired by the laser focused on the center of the strip. The isolated impulsive peaks refer to the breakages of single knitted microfilaments (black and green colored), breakage of single microwires (red colored) while breaking of a single knitted microfilament followed by a train of microwires failures are blue colored. The inset shows the frames extracted from a video recorded during the tensile testing of a PET net extracted from the composite strip. The frames were selected to highlight the case of failure/sliding of independent microwires forming a knitted microfilament; (e) Picture of the experimental setup highlighting the suspended PVDF web, the clamped sample for tensile testing, the commercial microphone and the laser vibrometer focused on the sample.

(e.g. Fig. 2(a)). The analysis of the sample morphology during testing, combined with experiments conducted at varying loading speeds, the simultaneous recording of induced vibrations and emitted sound, and the investigation of the failure mode of a pure PET net extracted from the PE matrix, revealed the complex intrinsic mechanisms governing composite strip vibrations. The load-bearing capacity of the system is primarily supported by the PET net, which elongates in the direction of the applied load until filament failure occurs. Morphological analysis, as shown in Fig. 3, reveals the hierarchical microstructure of the PET net that is formed by a regular grid of longitudinal and transversal filaments. In the longitudinal direction, the filaments consist of bundles of three knitted microfilaments, each made up of 16 PET microwires with a diameter of 16 µm (as depicted in Fig. 3 (c)). The knitting architecture forms a chain of elongated rings consisting of long, slender legs and high-curvature loops. Inde-

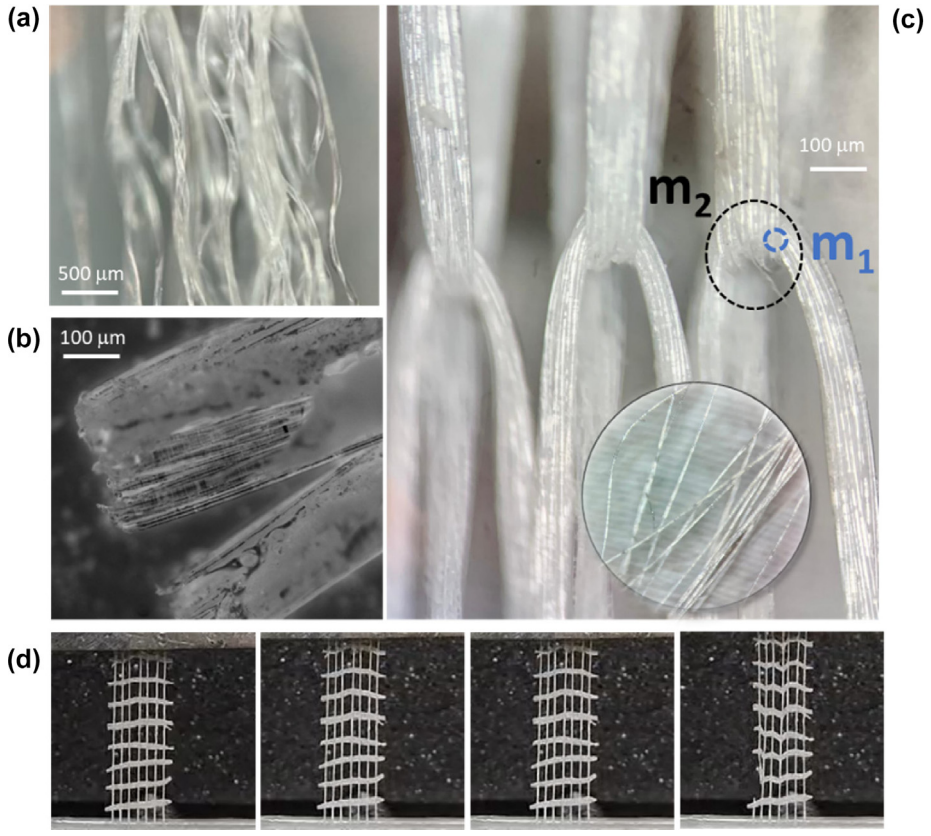

FIG. 3

Optical microscope images of the PET net architecture and hierarchical structure of the forming microfilaments. The net was disassembled from the PE composite strip by placing the strip on a petri dish and by pouring chloroform to form a bath. The solvent rapidly softened the adhesive layer, releasing the net in approximately 3 min, at room temperature. (a) Image of the transversal microfilaments that form the net show the aligned arrangement of the microwires; (b) Image of the failure section of a broken microfilament; (c) Image of a bundle of knitted microfilaments being each single knitted microfilament formed by the microwires pictured in the round inset. The image also highlights the architectural arrangement and the failure modes m_1 and m_2 via a light blue dashed-line circle (mode m_1) and a black circle (mode m_2), being m_1 the failure mode characterized by breakage of the microwires that form the knitted microfilament, and m_2 breakage of a single knitted microfilament formed by an assembly of knitted microwires; (d) Consecutive frames of a freestanding PET net (extracted from the matrix) while being loaded in tension. The last frame shows the first failure of a knitted microfilament.

pendent tensile testing of a PET net extracted from the composite strip reveals that, as the applied load increases, these bundles gradually elongate due to the extension of the rings along the loading direction. This process aligns the bundles perfectly with the applied load until failure occurs (as shown in Fig. 3(d) and the inset of Fig. 2(d)).

Failure consistently occurs in the sharp loop region of the chains, either as an apparently simultaneous rupture of the knitted microfilaments (last frame of Fig. 3(d)) or as sequential breakages of the microwires forming the microfilaments (third frame of Fig. 2(d)). Details of these failure modes are discussed later in conjunction with the vibration analysis. In the latter case, the failure of microwires is followed by their relative sliding, as clearly illustrated in the inset frames of Fig. 2(d).

The distinct failure features of the independent PET net dictate the failure mechanisms of the composite strip, as the net is anchored to the PE matrix. An initial failure of the outermost PET filament is recorded, leading to a localized reduction in load-bearing capability. This triggers significant local elongation of the embedding PE matrix, resulting in the formation of a neck along the corresponding edge of the composite strip. This necking occurs due to a V-shaped deviation of the transversal microfilaments, both observable in the insets of Fig. 2(a).

The neck formation signals the onset of matrix plasticization, which intensifies as neighboring filaments break. This plasticization is macroscopically identified by a localized whitening of the PE matrix, caused by the immediate alignment and sliding of its molecular chains. Subsequent filament breakages in the PET net drive the propagation of plasticization across the sample's width and towards the opposite edge. This continues until the PET net fully fails, and the composite strip's cross-section becomes completely plasticized.

Finally, the PE matrix tears, initiating from the region of the first filament failure, which experiences the highest strain level.

The described mechanisms, observable macroscopically through the consecutive frames in Fig. 2(c), govern the overall mechanical response shown in Fig. 2(a) and the force drops observed during local PET net failure. In general, the energy released during local failures induces vibrations in the composite strip, producing sound that carries specific phonetic signatures. As detailed in the analyses below, these vibrations (and the corresponding voicing mechanism) are influenced by: the breaking

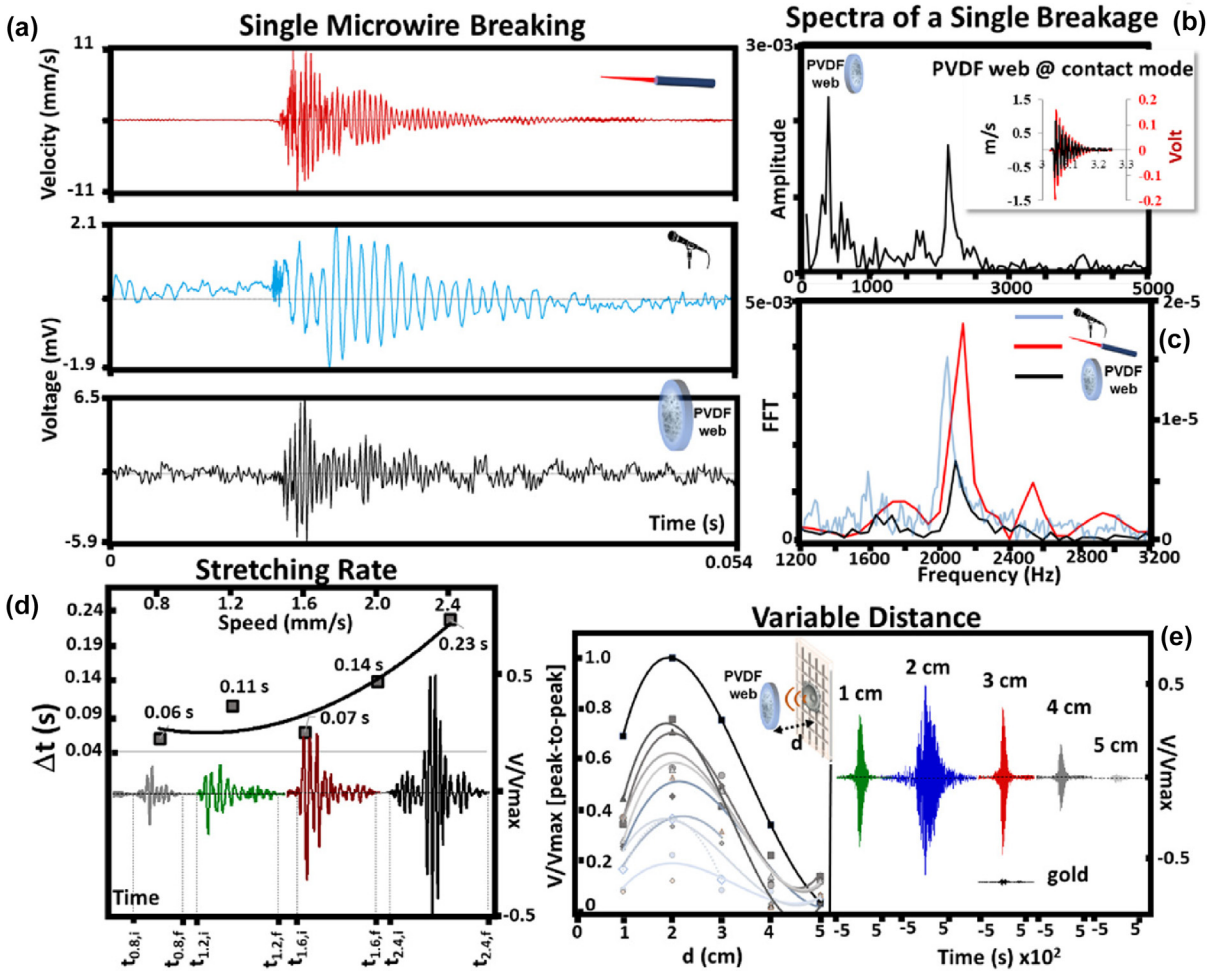

FIG. 4

Response of the three monitoring devices for the failure of a single knitted microfilament (failure mode m_2) referred to the third green peak in Fig. 2(d). The laser data in all graphs are reported in red color, the commercial microphone data are in blue color, while the piezoweb (PVDF web) data are in black color. (a) From top to bottom: laser, commercial microphone and PVDF web. The laser response is reported in terms of velocity, with a sampling rate of 9.76 μs and with a maximum impulsive action that reaches 10.71 mm/s. The commercial microphone with an acquisition rate of 5.2 μs shows a distorted travelling wave packet with a maximum initial impulsive peak of 3.5 mV. The piezoweb is also capable to detect the impulsive action with a maximum acquired raw voltage of 6.5 mV. (b) FFT of the piezoweb for the single microfilament failure in which three dominant peaks can be distinguished at 363 Hz, 2091 Hz and 4045 Hz. The inset shows the free vibration response (as voltage vs. time) of the piezoweb once surface mounted on a glass fiber composite cantilever actuated with an impulsive mechanical action. The response of the laser focused on the free edge of the cantilever is also reported for comparison in terms of velocity vs time. (c) FFT of the three devices (laser, commercial mic and piezoweb) for the second peak analyses. The commercial mic reaches the second resonance at 2044 Hz, the laser reaches resonance at 2133 Hz, while the piezoweb sets its resonance at 2091 Hz. (d) Stretching rate analysis in the time domain. Top panel: time window of the maximum sound signal for each loading speed (strip-to-piezoweb distance: 2 cm). The corresponding values at each speed are fitted with a second order polynomial fit. Bottom panel: sound signal for each speed (filtered data). The plotted signals are representative of those with the maximum amplitude among all detected failures (per loading rate). Left to right signals at: 0.8 mm/s, 1.2 mm/s, 1.6 mm/s, 2.4 mm/s with corresponding time-windows $(t_{0.8,f} - t_{0.8,i})$, $(t_{1.2,f} - t_{1.2,i})$, $(t_{1.6,f} - t_{1.6,i})$, $(t_{2.4,f} - t_{2.4,i})$, plotted as V/V_{max} over time, where V is voltage evolution over time and V_{max} is the peak at 2.4 mm/s. (e) Variable distance. (Left panel) Peak-to-peak amplitude with distance d from 1 cm to 5 cm (raw signal). The markers represent the maximum amplitude of each single peak, fitted with second order polynomial. (Right panel, filtered signal) V/V_{max} vs. time, labeled with distance values, where V_{max} is the maximum amplitude recorded among all distances for that specific impulse (namely 2 cm). The gold-coated piezoweb is tested at a piezoweb-to-loudspeaker distance of 3 cm.

mode of individual microfilaments (single microwires vs. knitted microfilaments), the degree of local stretching/plasticization of the PE matrix, and the loading speed. It is observed that direct vibration/sound monitoring is a valuable tool for analyzing the failure mechanisms. The velocity vs. time signal, monitored with a laser vibrometer focused at the center of the strips, in fact exhibited distinct peaks starting from approximately 17 % strain, recorded before global failure even in strips that failed suddenly. These peaks correspond to vibrations of the strip induced by the breaking of microfilaments, over time.

The impulsively induced vibrations in the composite exhibit distinct features. In Fig. 2(d), the black and green-colored peaks represent purely impulsive actions, reaching a maximum peak-to-peak value of 27 μm/sec. This mechanism corresponds to

the breakage of a single knitted microfilament, referred to as failure mode m_2 (highlighted in the inset in Fig. 3(c)). Instead, the blue-colored peaks show an initial impulsive peak (m_2 mode) followed by smaller consecutive peaks occurring every 20 μsec to 23 μsec, with a maximum peak-to-peak amplitude ranging from 2 μm/sec to 8 μm/sec. The smaller peaks are associated with consecutive and independent failures of microwires forming a microfilament (failure mode m_1). Additionally, isolated low-amplitude impulsive actions (red peaks in Fig. 2(d)) are attributed to the sudden failure of single microwires within a microfilament. Closer examination of the high-amplitude peaks (black and green-colored) reveals that the velocity variation over time is not purely impulsive but consists of multiple peaks within an ultra-small time window, followed by consecutive wave packets (Fig. 2(b)). This vibration noise is attributed to hierarchical and densely packed impulsive ruptures of the microwires forming a single knitted filament.

The observed laser peaks are simultaneously captured with an ultra-light nanostructured piezoelectric web (PVDF web) that the authors recently demonstrated to be highly sensitive for sound monitoring [74,75]. The sensing mat was realized with an optimized electrospinnng process (Experimental Section) which delivers spontaneously polarized PVDF webs (also named as piezowebs) with a d_{33} coefficient of (22.77 ± 8.94) pC/N. The PVDF web's electroactive phases β and γ, as well as the amorphous phase α are identified through the corresponding FTIR spectrum's peaks (β phase: 840 cm^{-1}, 1276 cm^{-1}, 510 cm^{-1} and 1482 cm^{-1}; γ phase: 1232 cm^{-1}; α phase: 762 cm^{-1}) highlighted in Fig. 1(d). The calculated crystalline content [26], F_α, F_β, and F_γ of these polymorph phases is 12 %, 46 % and 42 %, respectively for a total electroactive phase F_{EA} of 88 % (Experimental Section). The XRD analysis (Fig. 1(c)) [26,78], corroborates the crystalline microstructure of the PVDF web, thus the formation of the α, β, and γ phases through the identification of the corresponding deconvoluted peaks. In particular, for the crystalline β-phase the sharp 20.30° peak ($X_\beta \sim 52.55$ %) refers to the sum of diffraction in the (110) and (200) planes, while the smaller 36.36° peak relates to the diffraction of the (310) plane. The broader peak at 18.50° of the (020) diffraction plane corresponds to the electroactive γ-phase ($X_\gamma \sim 44.90$ %). A relatively smaller peak that identifies the α-phase is highlighted at 17.99° for a $X_\alpha \sim 2.55$ %.

The scanning electron microscope (SEM) image of the fibers highlights their random distribution and assembly in a uniform 120 μm thick, porous web. The average fibers diameter was 7 μm. The PVDF piezoweb was assembled as acoustic sensor with the design logic in Fig. 1(c) in which two peripheral electrodes sandwich the web. In this way the central part of the nanostructured membrane is directly exposed to air pressure waves generated by the impulsive energy that is released by the failing knitted filaments.

The membrane was allowed to vibrate freely only out-of-plane, perpendicular to the wave fronts to be captured. It was mechanically suspended using four elastic elements fixed at the web's edges (see Fig. 1(a)). The piezowebs were slightly tensioned to ensure a flat configuration and precise orientation relative to the propagating wave-fronts. Reference symmetric wavefronts were detected using a commercial microphone. The PVDF microfibers that form the piezoweb, despite being in micrometer scale, form an array of nanopores that are randomly distributed over the web, making the web extremely light (0.15 g) without affecting its capability to capture the vibrations of the surrounding air particles. As a result, the pressure wave dynamically excites the PVDF microfibers that get charged up with a time-dependent charge that is directly related to the energy released by the breaking filaments. The voltage generated by the piezoweb is reported as a function of time, for a single breaking knitted microfilament (mode type m_2) and its response is compared with that of the commercial microphone and of the vibrating composite (Fig. 4**(a)**).

The three detected signals are perfectly synchronized, indicating that the impulsive input of the composite, captured through the laser output, transforms into the mentioned wave packet during flight. This packet is clearly evident in both the PVDF piezoweb and commercial microphone acquisitions. The unfiltered web signal appears more stable and sensitive compared to the microphone, although the microphone has a higher signal-to-noise ratio due to its internal conditioning system. Fig. 4 demonstrates that the PVDF piezoweb signal has higher fidelity than the microphone signal, if compared with the composite vibrations.

The web effectively detected low-energy sound from the vibration noise caused by scattered failures of microwires within rupturing knitted filaments, as illustrated in Fig. 2(b). This is notable given its small footprint and being stretched by elastic springs, factors that typically reduce its performance. Elastic springs dampen vibration amplitudes, while a small footprint limits the area exposed to acoustic waves [76].

The small size was chosen for localized damage detection. The commercial microphone does not exhibit the consecutive peaks characteristic of knitted microfilament failure (in the the time-domain). However, the microphone is highly sensitive to reflected wave packets, while these are lost within noise in the PVDF piezoweb response. This observation makes the piezoweb an even more powerful device for damage recognition. Laser acquisition was utilized to validate two crucial aspects. Firstly, it monitored the dynamic response of the composite caused by the breaking wires. Secondly, it confirmed that the signal output of the suspended piezoweb solely relates to the sound propagation from the vibrating composite (non-contact configuration), not the composite's vibration itself. This distinction was necessary as the piezoweb, being piezoelectric, could generate voltage output if directly mounted on the strip (contact configuration). The direct mounting on the composite strip would have altered the strip response since the two have comparable thicknesses. To demonstrate this, the response of the piezoweb in contact configuration was then compared with laser monitoring of a stiffer glass fiber sample, showing a close match in detected vibrations (Fig. 4(b)). The analysis of the sound signal acquired by the PVDF piezoweb, in the frequency domain, allows the identification of the frequencies that are activated upon the impulsive breakage of the micro-filament. The corresponding Fast Fourier Transform (FFT) of the signal is shown in Fig. 4(b) in which three main peaks at 364 Hz, 2,091 Hz and 4,045 Hz are clearly identified within a frequency range up to 5 kHz. The analyses of the

signals acquired from the laser and the commercial microphone, also highlight similar peaks. For instance, the comparison of the second peak of the FFT signal coming from all three devices can also be viewed in Fig. 4(c). The sound signal of the piezoweb is found to have a natural frequency that is closer to that of the resonating composite (2133 Hz) with respect to the microphone output which is near 2,044 Hz.

The effect of loading speed on composite strip vibrations and the associated voicing mechanism (discussed in section 3) was examined. Increasing loading speed resulted in a higher rate of hierarchical failures within the microfilament structures (Fig. 4 (d)), causing denser ruptures and partial sound overlap in the time-domain. This led to signal broadening (Δt), increased vibration noise due to scattered failures, and amplified piezoweb volt-

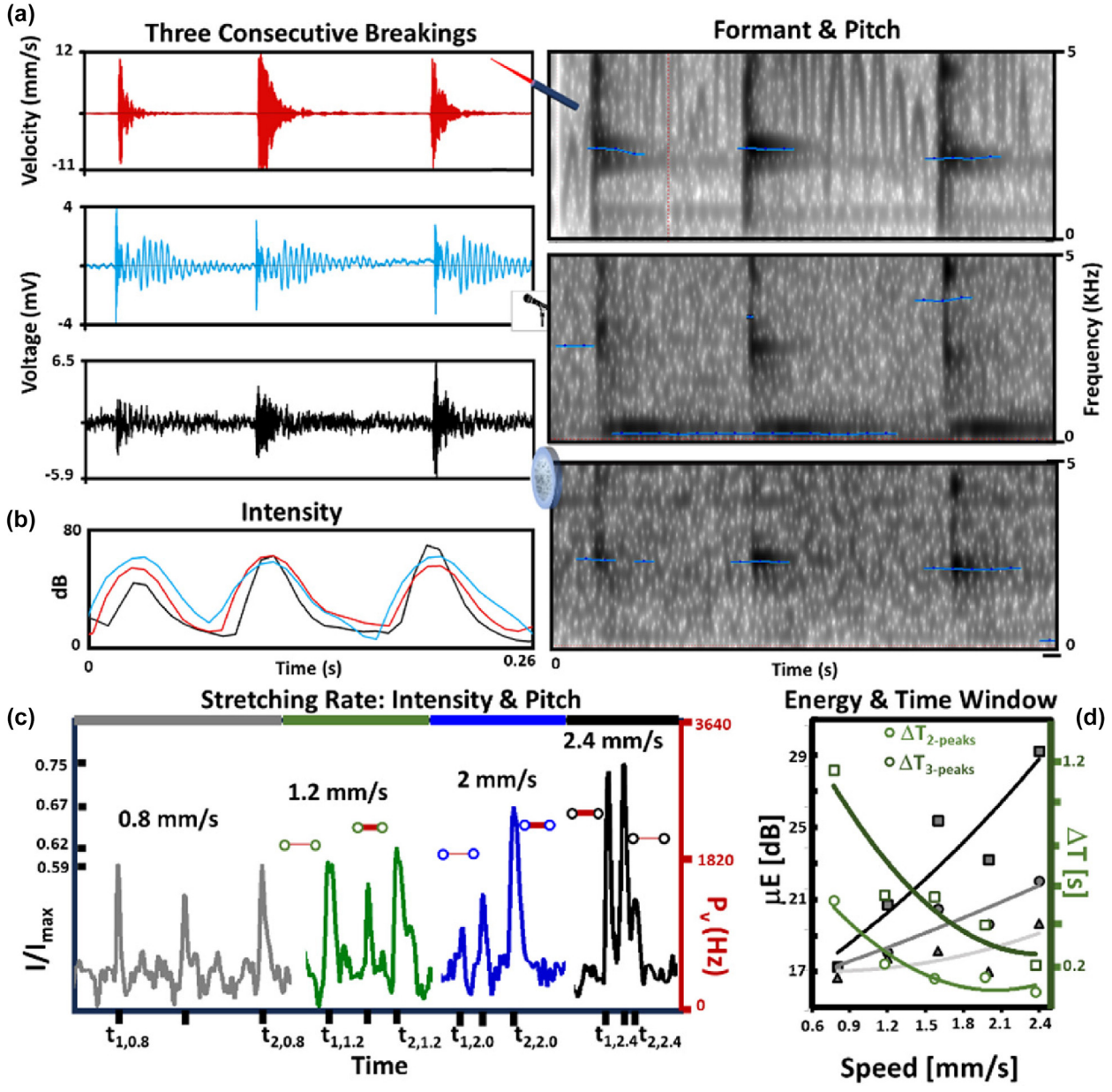

FIG. 5

Monitoring device responses for multiple filament failures in the time domain. (a) Laser, commercial microphone, and PVDF piezoweb from top to bottom (left column), with corresponding spectrograms (right column). Laser peaks: 10, 12, 10.7 μm/sec. Microphone peaks: 4.3 mV, 3.3 mV, 2.9 mV. Piezoweb peaks: 6.5 mV, 2.4 mV, 3.8 mV. Formant analysis in grey-scale map, pitches in light blue on spectrogram. (b) Intensity contour in dB for the three peaks. Devices synchronize with breaking events. Laser intensities: 39.33 dB, 44.91 dB, 40.18 dB. Microphone intensities: 30.97 dB, 28.6 dB, 29.8 dB. Piezoweb intensities: 72.14 dB, 75.56 dB, 76.75 dB. (c) Intensity and pitch of three rupturing filaments across stretching rates (0.8 mm/s to 2.4 mm/s, raw data). Intensity I normalized to I_{max} among the full multi-breakings events (29.24 dB at 2.4 mm/s) with a peak-to-peak voltage of 2 mV. The peaks occur at times $t_{n,m}$, (n = 1, 2, 3, m = index of loading rate). Two Pitch values P_V are graphed per rate: average (bolt red line) and mean (thin red line). Colors denote the loading rate, matching intensity contours. (d) Energy intensity (gray scale) and time window (green scale). Black markers and trendlines show, for each speed, energy intensity (square), mean energy intensity (circle) and mean intensities average of three consecutive peaks (triangle). Green markers and trendlines show time window for three (square) and two (circle) consecutive peaks.

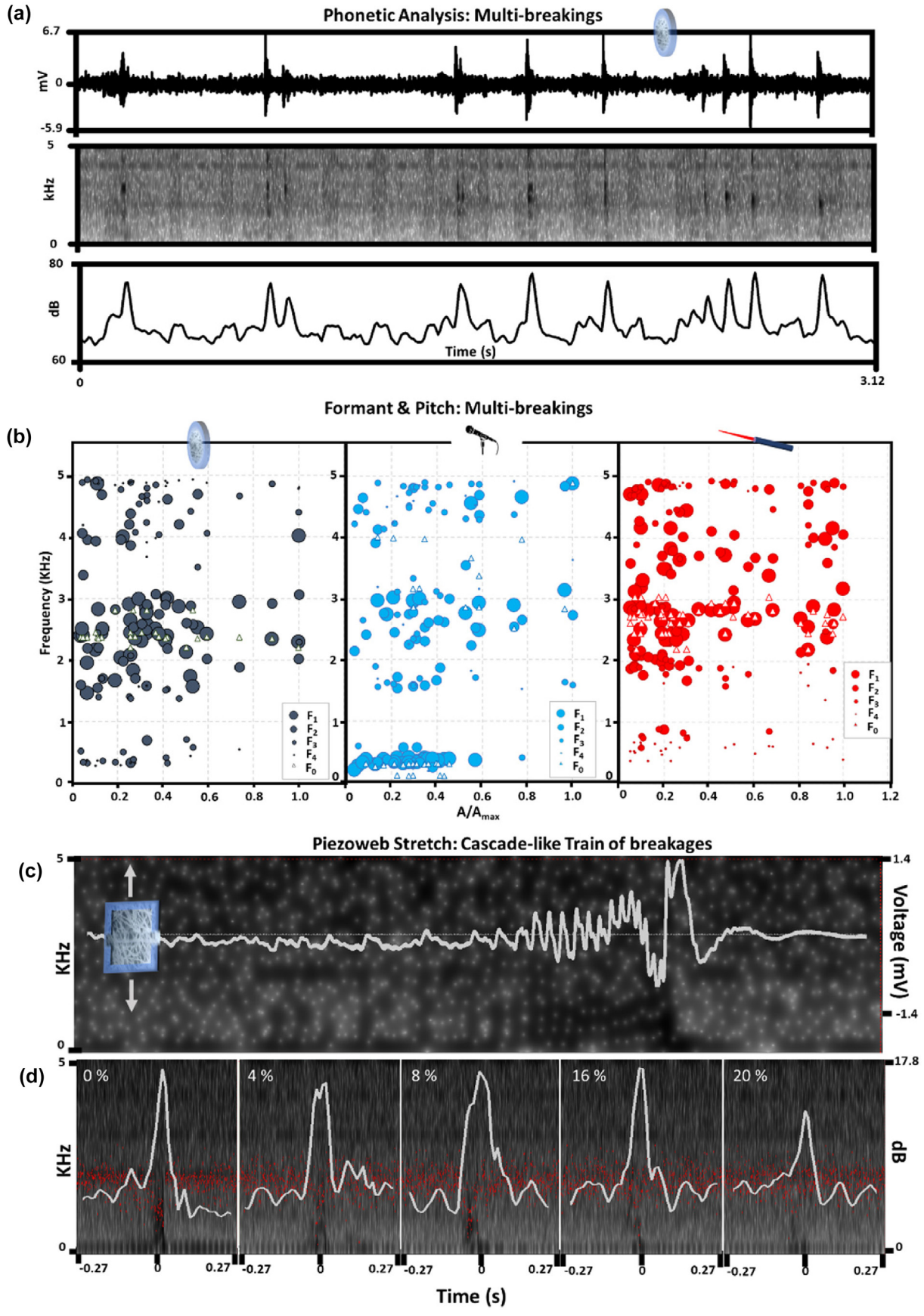
(a)
Phonetic Analysis: Multi-breakings
6.7
mV
0
-5.9
5
kHz
0
80
dB
60
Time (s)
0
3.12
(b)
Formant & Pitch: Multi-breakings
Frequency (KHz)
A/A_max
F1
F2
F3
F4
F0
(c)
Piezoweb Stretch: Cascade-like Train of breakages
KHz
Voltage (mV)
1.4
-1.4
(d)
0 %
4 %
8 %
16 %
20 %
KHz
dB
17.8
-0.27
0
0.27
Time (s)

age *V*. The Δ*t* vs *loading speed* showed a 283 % increase from 0.8 mm/s to 2.4 mm/s (412.5 % variation in peak-to-peak signal amplitude, Fig. 4(d)). Time-domain signals in terms of *V/Vmax* are depicted in Fig. 4(d) for each loading speed, with V_{max} representing the maximum peak-to-peak voltage among all speeds (e.g., 2.4 mm/s).

The capability of the PVDF piezoweb to detect multiple and indeed consecutive breakings of the knitted microfilaments is highlighted in the study as reported in the example in Fig. 5 in which again the web response is compared with that of the other two devices. The graphs represent the named purely impulsive breakages and refer to the consecutive green colored peaks in Fig. 2(d).

The frequency-domain is investigated in terms of spectral evolution over time which was necessary to avoid the overlap of impulsive signals coming from the independent breakage of the filaments. Each breaking microfilament was found to produce a similar output in terms of composite vibration and of sound signal in the time domain as well as in the frequency-domain. Higher energy densities are observed in the same ranges discussed for the single peak study with a dominant frequency near 2,000 Hz. The free oscillations of the vibrating composite show that higher energy densities are reached in an ultra-narrow time window, while the detected sound signals, that are related to a propagating acoustic sound, appear to be spread over a larger window due to the formation of the above-described wave packets. Similarly to the single peak analysis, the PVDF piezoweb is able to detect very clearly the hierarchical ruptures which occur, in an ultra-small-time step, for each of the three consecutive microfilament failures. The commercial microphone is again incapable to distinguish such highly dense micro-failures but is instead sensitive to the reflected wavepackets which are spread over a wide time-window. Such reflections are not clearly captured by the piezoweb due to the lower energy density content and to the unconditioned acquired signal. In conclusion, such results are showing that each single hierarchical filament, that has a similar morphological structure and mechanical response, gives rise, upon breakage, to a similar sound wave packet that carries in itself key information that are strongly related to the impulsive hierarchical action. Most importantly, these results highlight that the piezoweb can monitor such transient and indeed hierarchical and highly dense responses with ultra-high accuracy with respect to the commercial microphone, despite weighing less than 0.25 %.

Efforts were made to improve the amplitude of the PVDF piezoweb signal by analyzing the optimal distance of the piezoweb from the material to be monitored and by maximizing the acquisition of electric charges generated by the piezoweb when exposed to sound. Fig. 4(e) shows that the distance of 2 cm allows the wave packet to propagate and evolve reaching the maximum amplitude among the studied cases (Experimental section for details). V/V_{max} at 1 cm is 69 % than the 2 cm case, it drops down to 4.2 % at 5 cm, and is nearly indistinguishable with respect to background noise at larger distances. The trend is consistent for the full train of acoustic impulses (right panel). The extension of the peripheral Al electrodes in the central area was detrimental since the film, being stiffer and mechanically independent, disrupts the spontaneous evolution of the wave packet. The electrification of the web with a 50 nm Au layer didn't provide electrical continuity (1.2 KΩ across the sputtered area), the acoustic signal was unvaried. The 100 nm layer (Fig. 4(-e)-right panel), which ensured the porosity of the web at a relatively low electrical conductivity (6 Ω), showed a dramatic reduction in V/V_{max} (4.7 % with respect to the uncoated web) due to an increase in the fibers stiffness, hindering their effective deformation in response to the vibrating air particles.

The material phonetic

Deeper and indeed unconventional analyses were then carried out to investigate if the acquired sounds embed the fingerprints of this specific failure mode in terms of material speech. With such a logic, the detected sound signals generated by the filament's failure are reinterpreted as speech waves.

In the science of human speech, formants represent one of the key parameters to be analyzed. The vocal cords, by vibrating, modulate air flow produced by the lungs and generate sound. This sound is then shaped by the vocal tract to produce the phonetic sound which is at the base of human speech. The interesting aspect is that the sound source always produces the same sound signal, which is perceived differently thanks to the filtering action of the vocal tract that adapts its shape correspondingly to the sound to be emitted. In other words, the formants in human speech are related to the shape of the vocal tract and, to some extent, not to the source emitted by the vocal cords: formants represent the acoustic resonance of the vocal tract. Transferring this logic into materials, the source can be reinterpreted as the incipient damage and the material that is being damaged can be viewed as the vocal tract. Each material is characterized by its

FIG. 6

Phonetic analysis of the PVDF piezoweb response during multi-breaking events and stretching under a train of breakages: (a) Time domain response (amplified and rescaled), Formant's analysis and Intensity contour. Peaks range from 2.5 mV to 6.7 mV, with intensity modulating between 63.77 dB and 77.28 dB (from the amplified signal). Formants shown in grey scale depict material speech modulation. (b) Comparison of phonetic response among devices and its dependence on the characteristics of the breaking events. Graphs plot F0 (triangular marker), F1, F2, F3 and F4 in terms of normalized peak amplitude with formants represented by circular markers decreasing in size from F1to F4. (c) Spectrogram and time domain analysis of PVDF piezoweb under cascade-like events (baseline for stretching analysis). Spectrogram displays raw data, time domain response filtered. Inset shows piezoweb shape and the arrangement of the electrodes for stretching. (d) Piezoweb spectrograms at strains: 0 %, 4 %, 8 %, 16 %, 20 % with corresponding intensity contours (raw data). Formants range: 200 Hz to 1391 Hz (0 % strain), 368 Hz to 1525 Hz (4 % strain), 200 Hz to 1558 Hz (8 % strain), 234 Hz to 1508 Hz (16 % strain), 280 Hz to 1592 Hz (20 % strain). Maximum [and mean] intensity: 32.33 dB [26.4 dB] (0 %), 26.4 dB [23.2 dB] (4 %), 27.1 dB [22.9 dB] (8 %), 27.78 dB [22.18 dB] (16 %), 23.56 dB [20.62 dB] (20 %).

own frequency spectra and the impulsive release of energy due its local internal failure may selectively activate specific frequencies which are then captured by the PVDF piezoweb in terms of propagating sound. It seems clear that the impulsive action has a key role since its fingerprints can modify the activated frequencies in the material. In conclusion the impulsive action due to the occurrence of incipient damage excites specific acoustic resonances of the material and such excitation, that is monitored through the produced sound wave packets, carries in itself the fingerprints of the source and of the material. The analysis of the propagating sound and its reinterpretation in terms of material speech thus represents a precious source which can give key information about the material health. Phonetic analyses applied to materials were performed on the monitored wave packets with the support of PRAAT software [77]. The corresponding results are reported in Fig. 5 in terms of formants, intensity and pitch, for the consecutive filaments breakages reported in the same Figure. It is worth noting that such analysis has no claim of being an in-depth study related to the phonetic of materials but has the sole scope of highlighting its great potential of using the standard phonetic tools to reinterpret the material response in terms of its own spoken language. The data reported in Fig. 6 refers to the sound signals acquired by the PVDF piezoweb during the entire tensile response of the composite strip, up to its total failure.

The formants analysis is reported in terms of frequency vs. time, plotted as grey-scale spectrogram (see Fig. 6(a)), in which the three acoustic resonances of the composite, F1, F2 and F3, can be observed in terms of darker bands.

Such darker zones are clearly identified in this case study and their positioning along the time scale is in perfect agreement with the peaks of the voltage vs. time response captured via the PVDF piezoweb as depicted in the same Figure. This means that the phonetic analysis is a powerful tool to reinterpret the electromechanical response of the PVDF piezoweb as well as the material's health changes. The analysis of the intensity trend is also found to be in great agreement with the sudden breaking filaments, highlighting globally, an intensity level that is directly related to the corresponding failure mode. For instance, the microfilaments failure (m_1 mode), are characterized by intensity values within the extremely narrow range of 34.22 dB to 34.92 dB. A better view of the darker bands along the spectrogram, which occurs upon breakage of the filaments, is pictured in Fig. 5(a) for the case of the above discussed three consecutive microfilaments failure. The gray-scale map identifies very clearly the concentration of acoustic energy consistently over 2 KHz for all three devices and, the average F1, F2 formants of the three consecutive peaks are 2455.3 Hz/4499 Hz, 2411 Hz /4441 Hz and 3310 Hz/3770 Hz for the laser, piezoweb and microphone respectively. These formants values highlight the greater accuracy of the PVDF piezoweb to monitor the phonetic fingerprints with respect of the commercial microphone. The superiority of the piezoweb is also further corroborated by observing that the composite vibration and the piezoweb show dominant energy concentrations within an upper frequency range for the full time-window excited by each failing microfilament (within 11 ms and 23 ms for the piezoweb, and 16 ms and 34 ms for the laser vibrometer). Instead, the microphone's energy focuses in the upper frequency range just for the instantaneous impulsive action that is recorded by the microphone, which corresponds to a total time frame of 1.8 ms, an order of magnitude lower time-window than that of the other devices. The energy concentration of the microphone then dramatically drops down to ultra-low energy density levels that are carried by the mentioned reflected wavepackets that dominate this device response, stabilizing the F1 values at 317 Hz.

As highlighted earlier, the sample was chosen strategically to guarantee a sole type of rupture within the material which should deliver similar fingerprints of incipient damage in the phonetic analysis, a necessary step to validate the reliability of the proposed approach. The above discussed analysis of the filaments failure in the time-domain was useful to depict the hierarchical and multi-modal failure mechanisms that characterize the sample. It was observed that such impulsive failures release different amounts of energy providing a wide range of peak-to-peak amplitudes scattered in the time domain. To understand if the phonetic fingerprints are related to the amplitude of the mechanical impulse (in the time-domain), the phonetic analysis was extended to the full time-history which comprises the full spectrum of impulsive ruptures. The three formants (F1, F2 and F3) of all rupturing filaments are then analyzed in terms of the A/Amax ratio, being A the amplitude of the impulse and Amax the amplitude of the maximum recorded impulse over the full time-history. The corresponding analysis is reported in Fig. 6(b) for the PVDF piezoweb, the commercial microphone and for the laser signal that is used as reference. The size of the dots in each graph is related to the specific Formant being monitored. For instance, larger dots refer to F1, while the smallest dots refer to F4, thus F2 and F3 are gradually sized in between these two maximum and minimum values. This type of representation is helpful to easily visualize the overall formants dependence on the type of impulsive action. It is found that the piezoweb and the laser cover a larger spectrum of frequencies for failures that are characterized by lower impulsive amplitudes (A/Amax < 0.22). The formant F1 mainly falls within 1400 Hz and 2989 Hz, for the piezoweb and within 1683 Hz and 3314 Hz for the laser vibrometer, both populating just occasionally the upper frequency spectrum. The formant F2 instead dominates the upper frequency region within 3870 Hz/3420 Hz up to 5 KHz for the piezoweb/laser respectively. The formants F3 and F4 are mostly characterized by ultra-low frequencies below 1 KHz, setting a minimum at 290 Hz for the piezoweb and 370 Hz for the laser. With increasing A/Amax both devices show that the F1, F2 and F3 formants gradually populate mostly the upper frequency spectrum with the F1 and F2 formants more densely packed within 2 KHz and 3 KHz, while F4 sits mostly in the low frequency region. The apparent difference between the two plots is related to the lower amount of peak data that could clearly be analyzed through the unconditioned PVDF piezoweb signal. The microphone formants as a function of A/Amax instead highlight major differences with respect to the reference laser data especially for A/Amax below 0.6. The major difference is related to ultra-low F1 formants that for the microphone are mostly recorded between 199 Hz and 402 Hz which is an order of magnitude lower than that recorded by the piezoweb and the laser. Such a dramatically different response is related to the lower sensitivity

of the microphone in detecting and depicting the impulsive low-energy sound coming from the scattered failures of the microwires that are characterized by peaks that occur in consecutive sub-μs steps.

The acoustic periodicity in terms of pitch was also investigated through an autocorrelation method [51]. The interesting aspect of the pitch study is that its digits are solely related to the incipient damage. Pitch is in fact a measure of the vibration speed of the source. Higher pitches usually indicate rapid oscillations versus lower pitches indicate slower oscillations. The extremely irregular waveform pattern due to the sudden and scattered microfilaments failure is, to some extent, similar to those spoken languages in which some tones lower, rapidly shifting to radically different periods. In these languages the waveform does not follow a real periodic pattern, as in the case of microfilaments failures. The material is thus considered to be in "silence" during undamaged mechanical stretching, instead it "speaks" when it suddenly damages. This assumption leads to the concept that the large number of failing microwires, that release energy in a wide range, can be reinterpreted as a nonperiodic and scattered train of voiced/unvoiced patterns. In the sound of speech voiced/unvoiced patterns characterize radical transitions that might occur for instance through accidental strong voiceless (or voiced) sound with respect to a voiced (or voiceless) part. Such transitions are phonetically analyzed by tuning the voiced/unvoiced cost: higher costs decrease the number of transitions, and, oppositely, lower costs increase such a number [51]. The unique features of the sound emitted by the material are thus analyzed in terms of pitch by widening the pitch range to 5KHz and by adopting a voiced/unvoiced detection cost of 0.14μ to increase the number of acceptable voiced/unvoiced transitions. Such a cost is three orders of magnitude lower than that used for human speech. The corresponding pitches detected for the three devices are reported on the spectrogram as light blue lines for the three consecutive peaks in Fig. 5. The PVDF piezoweb pitches (1st: 2449 Hz, 2nd: 2395 Hz, 3rd: 2203 Hz) are in great agreement with those of the laser (1st: 2451 Hz, 2nd: 2449.9 Hz and 3rd: 2196.4 Hz). Instead, the microphone pitches within a similar range could be detected only by analyzing the ultra-small-time window of 0.1 ms to 0.2 ms that corresponds to the wave front that reaches first the microphone and by fine-tuning the silence and voicing threshold as typically done in speech analysis to overcome background noise. Fig. 5 in fact shows that outside this window the pitches set to ultra-low values, in perfect agreement with the overall microphone spectral and time-domain response. Despite the implementation of ad-hoc strategies for the microphone analysis, according to which the voicing threshold is lowered to 0.045, the detected microphone pitches (1st: 2511 Hz, 2nd: 3372 Hz, 3rd: 3648 Hz) diverge from those of the laser and piezoweb. The analysis of the pitch as a function of peak amplitude variation is reported in Fig. 6(b) in which the pitch F_o values are represented by triangular markers. It is observed that pitch doesn't seem to change with the peak amplitude, an average 2649.5 Hz, 2426 Hz and 3409 Hz is in fact measured for the laser, piezoweb and microphone, respectively. This result is in perfect agreement with the concept that pitch refers solely to the speed of the sound source which, in this case study, is of the same nature for each breaking event since failure of the hierarchical filaments is the sum of a number of identical to-each-other microwires which should deliver similar fingerprints of the source. In principle, just the energy release is expected to change, since it is related to the number of microwires failing simultaneously, in cascade or with a pause, delivering an overall voiced/unvoiced sound pattern. The analysis of the pitch in terms of progressive failures shows however an indeed interesting trend for the PVDF piezoweb and the laser. The fundamental F_o frequency is in fact found to progressively decrease with increasing number of filaments failures. An overall 28 % and 22 % pitch decrease is respectively detected for the laser and the piezoweb. This result can be explained by considering that, while in humans the vocal cords act independently from the vocal tract that changes shape to modulate the sound emitted by the cords, in the composite case the breaking filaments, that play in the material the same role of the vocal cords, to some extent are affected in their vibration speed by the hosting material whose local rigidity impulsively decreases with increasing consecutive failures, as discussed in Fig. 2(a). In other words, the vocal tract of the material changes progressively and "permanently" in the case of a failure test and this affects the actuation speed of the embedded material's vocal cords that correspondingly decreases. The permanent phonetic changes of the material are in fact demonstrated through the PVDF piezoweb and laser that respectively reported a 21 % and 5 % decrease in first formant (F1) when comparing the initial and ultimate filaments failures. The microphone response instead didn't show the same clear logic in the recorded mechanical and phonetic data.

Finally, the intensity contour that is related to sound power and is expressed dB as loudness, shows that all filaments, while breaking, induce a sound pressure level that is related to the failure mode. The intensity plot of the three consecutive peaks in Fig. 5(b), shows in fact a similar trend since all three failures refer to mode m_2. The intensity contour of the full failure test, that is reported in Fig. 6(a) for the piezoweb case, highlights that the intensity module is in perfect agreement with the recorded time-history and impulsive actions.

Analyzing voicing mechanisms under varied loading speeds (Fig. 4(d)) reveals a key finding: faster speeds accelerate filament breakage, narrowing the time window for rupturing events, resulting in fused voiced/unvoiced transitions thus to heightened peak intensities. However, intensified local peaks may not directly correlate with an overall increase in mean energy release during multi-breaking events. The mean energy release varies with loading speed at a lower rate than isolated peak intensities, indicating a strong dependency on the material's molecular structure rather than molecular rearrangements, which are limited under rapid loading. Additionally, the study suggests a slight correlation between loading speed and vocal cord vibration speed (pitch). The described voicing mechanism is well-supported by experimental findings. In Fig. 5(c), the increase in energy intensity due to the overlap of the voiced/unvoiced transitions is evident across consecutive breakages at various speeds. Additionally, Fig. 5(d) illustrates energy and mean energy intensity changes of the maximum peak within multi-breaking events at different speeds. For instance, the maximum intensity rises from 17.26 μE (dB) to 29.24 μE (dB) as speed increases from 0.8 mm/s to 2.4 mm/s, with corresponding time windows rang-

ing from 542 μs to 95 μs. Mean peak intensities reach 22.05 μE (dB) at the maximum loading rate. In Fig. 5(c), a modest rate of increase is observed by averaging the mean intensity of the three consecutive peaks across different loading speeds: 16.6 μE (dB) and 19.7 μE (dB) at the lowest and highest speeds, respectively. The latter finding supports the stronger influence of the material's molecular structure on overall mean energy compared to loading speed. Additionally, the three consecutive peaks exhibit minor pitch variations with increasing speed. For instance, an average 2392 Hz (SD 34) and 2220 Hz (SD 100), representing a 7 % decrease in pitch, are recorded at loading speeds of 2.4 mm/s and 1.2 mm/s (100 % speed variation), respectively. These pitch changes may be linked to modulus increases with loading speed (482.5 MPa and 466.23 MPa at 2.4 mm/s and 1.2 mm/s, respectively), resulting in faster increase in the filaments' frequency (being $f = \frac{1}{2\pi}\sqrt{\frac{K}{m}}$) causing an increase in particle's velocity, thus of pitch.

The analysis of the voicing mechanism, particularly understanding the links between intensity, pitch, material's molecular structure, integrity, and mechanical parameters (e.g., stiffness), confirms the reliability of the proposed phonetic approach in detecting the material's fingerprint towards material's speech.

The great quality of the sound perceived by the fibrous web was reproduced and recorded. The corresponding sound can be appreciated playing the audio file included in the supporting material.

The study aims to explore the PVDF piezoweb's potential in detecting phonetic fingerprints while stretched, envisioning its coupling with sound-emitting materials. Fig. 6(c) illustrates the piezoweb's response during strip tearing, as detailed in the Experimental section.

Induced breakages are evident from consecutive peaks in the time-domain response and corresponding darker areas in the gray-scale spectrogram. These breakages, occurring within an ultra-small time window (on average 143 μs for full strip failure), resemble a cascade of failing microfilaments. Such rapid ruptures result in overlapping emitted sounds, phonetically represented by a global intensity contour rather than isolated peaks for each breaking microfilament. This suggests that contour analysis captures the full energy intensity spectrum emitted by the breaking strip. Fig. 6(d) shows intensity contours for increasing piezoweb stretching. Interestingly, stretching the piezoweb doesn't significantly affect its ability to capture the material's acoustic properties. Only a 16.2 % variation in maximum intensity and a 13.8 % variation in mean intensity are detected when stretching the piezoweb up to 16 % strain.

The absence of a clear intensity trend with stretching, coupled with piezoweb morphology inspection at each degree of stretching, indicates energy intensity changes are mainly due to local triboelectric contact loss between Al electrodes and the piezoweb. Triboelectric loss increases at 20 % strain, resulting in a 27.8 % intensity decrease.

The spectrograms in Fig. 6(d) illustrate the piezoweb's ability to detect the fingerprints of rupturing filaments at different stretching levels, despite a decrease in acquired charges. Darker bands indicate formants from 200 Hz to 1391 Hz in the unstretched web. Increased web stiffness with stretching enhances sensitivity to higher frequencies, widening the formant frequency window. At 20 % strain, the upper value shifts to 1592 Hz (further details in figure caption). Analysis focuses on frequencies below 1700 Hz to avoid interference with setup noise (see inset, Fig. 6(c)).

Conclusion

The work presented in this paper shows for the first time in literature that sound signals generated from materials can be reinterpreted in terms of material's speech. The detected sounds encode in themselves speech-related information that can be used to assess, among other things, the material health state. This finding represents a seed toward the conceptual idea that materials can embed humanoid functionalities. In such a frame of mind, the usage of ultra-light-in-weight microphones, as the nanostructured web presented in this study, is necessary to capture and reinterpret the energy that is released from the materials.

Experimental section/methods

PVDF powder (1.9 g, 534Kgmol^{-1}) (Sigma Aldrich), was mixed with 3 mL of DMA (N, N-dimetilacetammide) and 7 mL of Acetone, was heated (80° C) and magnetically stirred on a hot plate for 2 h, then was cooled to room temperature. *Electrospinning parameters*. needle-to-collector distance 12 cm, 12 KV, 0.8 mL/hr for 3 min, air drying for 30 min. Microscopic inspections to analyze structural uniformity, morphology, fiber and web thickness. *Crystallinity analysis*: electroactive/ non-polar phases were quantified with Nicolet Summit FTIR Spectrometer (Thermo Fisher-ATR mode) and with X-Ray diffraction analysis with XRD D8 Discover (Bruker) performed with Cu Kα radiation at 40 KV and 30 mA [26,78]. *Acoustic sensor assembly*. 8.5 × 8.5 c m^2 of PVDF web was sandwiched between two 6x8 cm^2 rectangular Al foil electrodes with a circular hole of 2.5 cm in diameter.

Commercial composite strips (Tesa R) (180 μm thick, 6 cm long, 1 cm wide) were tested in tension (at a temperature of 19 °C and 64 % humidity) with a slight tilt and 2.4 mm/s displacement control. The piezoweb was suspended at 3 cm. The oscilloscope signal was amplified a hundred times for the analysis, unless specified otherwise, analyzed data were remodulated to their unamplified values.

A pre-polarized omnidirectional condenser microphone (MelLab) was placed symmetrically opposite the composite. A Polytec laser vibrometer (MSA500) was orthogonally focused at the sample's center. Laser data, converted into an audio file using a MatLab script, was played through a speaker at distances ranging from 1 cm to 6 cm from the sensor.

A 50 nm and 100 nm gold layer were sputtered on the top and bottom of the piezoweb and were tested at a 3 cm distance from the speaker. Tensile tests were conducted on composites measuring 2 cm in length and 1 cm in width at 28 °C and 75 % humidity. Testing speeds varied from 2.4 mm/s to 0.8 mm/s, while the piezoweb monitored sound from a distance of 2 cm. The elastic modulus was analyzed by conducting tensile tests on

5 cm x 1 cm samples at different loading speeds. The piezoweb sensor, mounted on a tensile testing system with insulating strips, monitored the rupture of a composite strip placed at 2 cm. The test was repeated, gradually stretching the piezoweb up to 20 % strain. In this study, a 5 cm strip with a 5 mm pre-cut was horizontally clamped between rigid, electrically insulating plates and sheared at a high rate for rapid rupture (between 96 μs and 157 μs). The piezoweb sensor design was modified for stretching, involving: (1) square peripheral electrodes sandwiching a 2.5 cm x 2.5 cm membrane for uniform stretching; (2) As Al couldn't stretch, electrodes were divided in half, with flying electrical connectors to ensure charge capture.

The piezoweb was surface-mounted on a free-vibrating glass fiber composite cantilever (in contact mode), simultaneously monitored by a laser focused at the free tip.

CRediT authorship contribution statement

Giulia Lanzara: Writing – review & editing, Writing – original draft, Validation, Supervision, Resources, Project administration, Methodology, Investigation, Funding acquisition, Formal analysis, Conceptualization, Data Curation. **Krishna Chytanya Chinnam:** Writing – review & editing, Software, Methodology, Investigation, Data curation, Validation, Formal Analysis. **Erika Magnafico:** Investigation. **Federico Fabriani:** Investigation.

Data availability

Data will be made available on request.

Declaration of competing interest

The authors declare that they have no known competing financial interests or personal relationships that could have appeared to influence the work reported in this paper.

Acknowledgements

This research was funded by the Air Force Office of Scientific Research (AFOSR)/European Office of Aerospace Research and Development (EOARD), Award n. FA8655-20-1-7036 for which Lt Col David Swanson and Dr. Les Lee are gratefully acknowledged. The authors would also like to express their gratitude to Saqib Rashid for acquiring the XRD data and to Alessandro Porrari for his valuable support in the mechanical testing of the composite PE/PET strips. SEM images were acquired at the Inter-Departmental Laboratory of Electron Microscopy (LIME), Università degli studi Roma Tre (http://www.lime.uniroma3.it).

Appendix A. Supplementary material

The piezoweb and the laser signal are provided as audio files in supporting information (sensor sound.mp3; and laser sound.mp3). Supplementary data to this article can be found online at https://doi.org/10.1016/j.mattod.2025.01.003.

References

[1] S. Metaxa et al., Procedia Struct. Integrity 22 (2019) 369–375.
[2] Y. Yang, Y. Zhang, T. Xiaokun, Symmetry 2021 (1998) 13.
[3] Z. Wang, Y.-J. Cha, Eng. Rep. (2022) e12551.
[4] F. Angeletti et al., Sensors 23 (1) (2023) 368.
[5] M.M. Azad et al., Arch. Comput. Meth. Eng. (2024) . https://doi.org/10.1007/s11831-024-10146-y.
[6] P. Kot et al., Appl. Sci. 11 (6) (2021) 2750.
[7] R. Soleimanpour, S.M. Soleimani, N.K. Mohammad, Procedia Struct. Integrity 37 (2022) 956–963.
[8] O. Ahmed et al., Compos. B Eng. 223 (2021) 109136.
[9] X. Cheng et al., Sensors 22 (20) (2022) 7795.
[10] P. Jiao et al., Sensors 20 (2020) 3730.
[11] M. Boota et al., Sci. Technol. Adv. Mater. 17 (2016) 45–57.
[12] M. Boota et al., AIP Adv. (2016) 055303.
[13] V. Giurgiutiu, In Structural Health Monitoring of Aerosapce Composites, Academic Press, Elsevier, 2015 (Chapter 8).
[14] K. Bremer et al., Procedia Technol. 26 (2016) 524–529.
[15] H.H. Zhu et al., Sensors 22 (19) (2022) 7550.
[16] M.A. Rahman et al., Mech. Syst. Sig. Process. 208 (2024) 110983.
[17] D. Garcia, D. Tcherniak, Mech. Syst. Sig. Process. 127 (2019) 102–119.
[18] S. Li et al., Sensors 22 (3) (2022) 812.
[19] E. Magnafico, et al., in: Proceedings of the ASME 2019 Conference on Smart Materials, Adaptive Structures and Intelligent Systems 2019 Louisville, Kentucky, USA. September 9–11, 2019. V001T01A007. ASME.
[20] G. Formica et al., J. Appl. Mech. 86 (4) (2019) 041007.
[21] N. Shehata et al., Nanomaterials 8 (2018) 585.
[22] R.K. Singh, S.W. Lye, J. Miao, Sens. Actuators, A 303 (2020) 111841.
[23] F. Fabriani et al., Proceedings 2 (2018) 501.
[24] W. Guo et al., Nanoscale 10 (2018) 17751.
[25] Y. Wu et al., Mater. Des. 211 (2021) 110164.
[26] P. Martins, A.C. Lopes, S.L. Mendez, Prog. Polym. Sci. 39 (4) (2014) 683–706.
[27] M. Soha et al., RSC Adv. 13 (2023) 370–387.
[28] S. Im, S.D. Bu, C.K. Jeong, J. Korean Inst. Electric. Electron. Mater. Engineers 35 (6) (2022) 523–546.
[29] J. Park et al., Small 18 (2022) 2104472.
[30] P. Cawley, Struct. Health Monit. 17 (5) (2018) 1225–1244.
[31] Y. Wang et al., Struct. Health Monit. (2021) . https://doi.org/10.1177/14759217211056831.
[32] Z. Guo et al., Struct. Health Monit. 17 (3) (2018) 598–623.
[33] M.A. Mousa et al., Infrastructures 6 (2021) 176.
[34] A. Enshaeian, et al., in: Experimental Mechanics, vol. 61, 2021, pp. 705–718.
[35] Z. Azouz, B.H.S. Asli, M. Khan, Sensors 24 (18) (2024) 5871.
[36] R. Kromanis, P. Kripakaran, J. Civ. Struct. Heal. Monit. 6 (2016) 236–254.
[37] T. Miyashita, M. Nagai, Steel Struct. 8 (2008) 325–331.
[38] W.J. Staszewski et al., Smart Mater. Struct. 13 (2004) 251.
[39] A. Zabihi et al., Energies 17 (9) (2024) 2165.
[40] B. Wang, Z. Cheng, W. Liao, et al., Struct. Health Monit. (2024) .
[41] Z.W. Tham et al., Compos. Sci. Technol. 257 (2024) 110796.
[42] T. Sugimoto et al., Jpn. J. Appl. Phys. 63 (2024) 04SP45.
[43] G. Frusque et al., Mech. Syst. Sig. Process. 208 (2024) 111022.
[44] A. Sabato et al., IEEE Sens. J. 23 (5) (2023) 4672–4684.
[45] C. Krolovec, M. Schagerl, Sensors 20 (3) (2020) 826.
[46] M. Wevers, NDT&E Int. 30 (2) (1997) 99–106.
[47] A. Frendi, L. Maestrello, L. Ting, J. Sound Vib. 182 (1995) 741–747.
[48] M. Ruzzene, J. Sound Vib. 277 (2004) 741–763.
[49] M.C. Junger, Comput. Struct. 65 (1997) 287–293.
[50] E. Mucchi, A. Vecchio, Measurement 43 (2010) 283–297.
[51] H. Jiang, D.E. Adams, K. Jata, Struct Health Monit. 5 (2006) 373–387.
[52] V. Arora, Y.H. Wijnant, A. de Boer, Appl. Acoust. 80 (2014) 23–27.
[53] Y. Huang, Y. Yusuke, in: Proceedings of the 2024 New Zealand Society for Earthquake Engineering Annual Technical Conference, 2024.
[54] G. Sharma, et al., 2022 Second International Conference on Computer Science, Engineering and Applications (ICCSEA), Gunupur, India, 2022, pp. 1–5, https://doi.org/10.1109/ICCSEA54677.2022.9936438.
[55] J.G. Cherng, X.F. Chen, V. Peng, Measurement 18 (1996) 207–214.
[56] N.S.V.N. Hanuman, T. Bose, Strength Mater. 55 (2023) 1228–1239.
[57] F. Wei, Z. Ruohua, Z. Guo, Structures 55 (2023) 1774–1782.
[58] A. Baghalian, V.Y. Senyurek, S. Tashakori, et al., J. Nondestruct. Eval. 37 (2018) 24.
[59] F. Huda et al., IOP Conf. Ser.: Mater Sci. Eng. 539 (2019) 012034.
[60] P. Rzeszucinski et al., IEEE Ind. Appl. Mag. 24 (4) (2018) 17–23.
[61] L.A. Sergio et al., J. Bridg. Eng. 24 (2019) 5.
[62] O. Yapar et al., Eng. Fail. Anal. 56 (2015) 150–169.
[63] P. Poozesh et al., Struct. Health Monit. 16 (4) (2017) 471–485.

[64] C. Beale, M. Inalpolat, C. Niezrecki, Struct. Health Monit. 19 (1) (2020) 48–65.
[65] J. Solimine, C. Niezrecki, M. Inalpolat, Struct. Health Monit. 19 (6) (2020) 1711–1725.
[66] S. Sun et al., Struct. Health Monit. 22 (1) (2023) 201–215.
[67] Y. Zhu et al., Machines 10 (12) (2022) 1184.
[68] S. Ding, C. Yang, S. Zhang, Sensors 23 (11) (2023) 4987.
[69] Y. Bai, Y. Liu, G. Gao, et al., Acoust. Phys. 70 (2024) 130–142.
[70] C.N. Teague et al., IEEE Trans. Biomed. Eng. 63 (8) (2016) 1581–1590.
[71] H. Shintaku et al., Sens. Actuators, A 158 (2010) 183–192.
[72] Y. Jung et al., Sensors 14 (2014) 117–128.
[73] Y.H. Jung et al., Adv. Mater. 32 (2020) 1904020.
[74] K.C. Chinnam, G. Lanzara, In: Lcarbonara, W. (eds) Advances in Nonlinear Dynamics, Volume II. ICNA 2023. NODYCON Conference Proceedings Series, Springer, Cham, 2024. https://doi.org/10.1007/978-3-031-50639-0_21.
[75] K.C. Chinnam et al., Proceedings of the ASME 2023 Conference on Smart Materials, Adaptive Structures and Intelligent Systems, ASME 2023. Conference on Smart Materials, Adaptive Structures and Intelligent Systems, V001T04A017, September, Austin, Texas, USA, 11–13, 2023. https://doi.org/10.1115/SMASIS2023-111178.
[76] C. Lang et al., Nat. Commun. 7 (2016) 11108.
[77] P. Boersma, V. van Heuven, Glot Int. 5 (9/10) (2001) 341–345.
[78] X. Cai et al., RSC Adv. 7 (2017) 15382–15389.